Cell Reports
Methods

Report

Longitudinal *in vivo* monitoring of axonal degeneration after brain injury

Graphical abstract

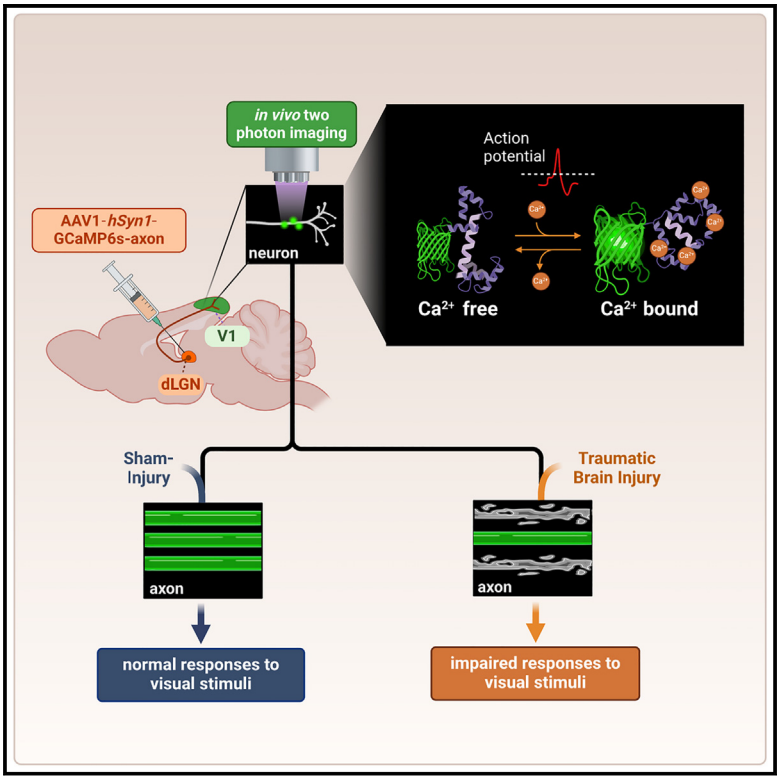

Highlights

- Repeated within-animal axonal activity patterns are recorded after brain injury
- Brain injury modulates axonal activity patterns
- Animal numbers are minimized by recording from the same axons
- The *in vivo* approach can be applied to basic science and therapeutic discovery

Authors

Sergiy Chornyy, Julie A. Borovicka, Davina Patel, ..., Brigid Wilson, Andrew A. Pieper, Hod Dana

Correspondence

andrew.pieper@harringtondiscovery.org (A.A.P.),
danah@ccf.org (H.D.)

In brief

Brain injury damages axons, causing chronic neurodegeneration. Studying axonal degeneration is challenging because traditional histological methods require large numbers of animals. Chornyy et al. develop a method that reduces the number of required animals by recording axonal activity within the same animal using nonlinear microscopy of genetically encoded calcium sensors.

Chornyy et al., 2023, Cell Reports Methods *3*, 100481
May 22, 2023
https://doi.org/10.1016/j.crmeth.2023.100481

CellPress

Cell Reports Methods

CellPress
OPEN ACCESS

Report

Longitudinal *in vivo* monitoring of axonal degeneration after brain injury

Sergiy Chornyy,[1] Julie A. Borovicka,[1] Davina Patel,[1] Min-Kyoo Shin,[2,3,4,5,6] Edwin Vázquez-Rosa,[2,3,4,5] Emiko Miller,[2,3,4,5,7] Brigid Wilson,[8] Andrew A. Pieper,[2,3,4,5,7,*] and Hod Dana[1,9,10,*]

[1]Department of Neurosciences, Lerner Research Institute, Cleveland Clinic, Cleveland, OH 44195, USA
[2]Harrington Discovery Institute, University Hospitals Cleveland Medical Center, Cleveland, OH 44106, USA
[3]Department of Psychiatry, Case Western Reserve University, Cleveland, OH 44106, USA
[4]Geriatric Research Education and Clinical Center, Louis Stokes Cleveland VA Medical Center, Cleveland, OH 44106, USA
[5]Institute for Transformative Molecular Medicine, School of Medicine, Case Western Reserve University, Cleveland, OH 44106, USA
[6]College of Pharmacy and Research Institute of Pharmaceutical Sciences, Seoul National University, Seoul 08226, Republic of Korea
[7]Department of Neuroscience, Case Western Reserve University, School of Medicine, Cleveland, OH 44106, USA
[8]Department of Infectious Diseases and HIV Medicine, Case Western Reserve University, School of Medicine, Cleveland, OH 44106, USA
[9]Department of Molecular Medicine, Cleveland Clinic Lerner College of Medicine, School of Medicine, Case Western Reserve University, Cleveland, OH 44195, USA
[10]Lead contact
*Correspondence: andrew.pieper@harringtondiscovery.org (A.A.P.), danah@ccf.org (H.D.)
https://doi.org/10.1016/j.crmeth.2023.100481

MOTIVATION Traumatic brain injury is characterized by chronically progressive axonal degeneration that leads to neuronal cell death and neuropsychiatric impairment. Current laboratory methods to assess axonal integrity rely on postmortem histological characterization and are thus unable to monitor axonal degeneration in the same animal over time. Moreover, studies over extended periods of time require exceedingly large numbers of animals. To overcome this limitation, we report here the development of a method for *in vivo* multiphoton microscopy of calcium sensors that enables longitudinal recording and quantification of functional axonal activity before and after injury at multiple time points in the same mouse.

SUMMARY

Traumatic brain injury (TBI)-induced axonal degeneration leads to acute and chronic neuropsychiatric impairment, neuronal death, and accelerated neurodegenerative diseases of aging, including Alzheimer's and Parkinson's diseases. In laboratory models, axonal degeneration is traditionally studied through comprehensive postmortem histological evaluation of axonal integrity at multiple time points. This requires large numbers of animals to power for statistical significance. Here, we developed a method to longitudinally monitor axonal functional activity before and after injury *in vivo* in the same animal over an extended period. Specifically, after expressing an axonal-targeting genetically encoded calcium indicator in the mouse dorsolateral geniculate nucleus, we recorded axonal activity patterns in the visual cortex in response to visual stimulation. *In vivo* aberrant axonal activity patterns after TBI were detectable from 3 days after injury and persisted chronically. This method generates longitudinal same-animal data that substantially reduces the number of required animals for preclinical studies of axonal degeneration.

INTRODUCTION

Worldwide, there are ~50 million annual cases of traumatic brain injury (TBI).[1] These typically entail acute and chronic complications, including visual deficits, post-traumatic stress disorder, cognitive impairment, and major depression. TBI also incurs tremendous annual healthcare costs, reaching $13.1 billion in the United States alone, with an additional $64 billion in lost productivity.[2] An early and chronic consequence of TBI is axonal degeneration, which impairs brain circuitry and leads to neuronal death.[3,4] TBI also increases the risk of aging-related neurodegenerative diseases,[5] including Alzheimer's disease (AD)[6] and Parkinson's disease (PD).[7] Although the mechanism for this link is unknown, axonal degeneration is thought to play a fundamental role in the process.[8] To meet the urgent unmet need for neuroprotective strategies to stop axonal degeneration, it is critical to evaluate putative therapies in preclinical models. However, long-term assessment of axonal degeneration using

traditional histological methods in animal models requires massive amounts of tissue for statistical power across a range of acute and chronic time points. By contrast, sufficient statistical power for longitudinal studies can also be achieved when repeated measurements are obtained from a much smaller number of animals.[9–11] Therefore, we developed a method of longitudinal monitoring of axonal integrity *in vivo* in the same animals over extended periods of time to provide a more efficient method of evaluating axonal degeneration.

Two-photon microscopy of the fluorescence signal from neurons expressing a genetically encoded calcium indicator (GECI) allows *in vivo* monitoring of neuronal activity over multiple weeks.[12–16] Most GECIs, such as the widely used GCaMP family of sensors,[13,17–19] increase their fluorescence signal upon binding to calcium ions and therefore become brighter when neurons fire action potentials and their intracellular calcium ion concentration increases. This brighter fluorescence signal is apparent across various neuronal components, including the soma,[13,17,19] dendrites and spines,[20] and axons.[18,21] We note that although several post-processing algorithms have been developed to extract action potential timing from GECI fluorescence traces,[22–25] they relied on somatic firing patterns, and axonal transients were not validated. Therefore, we did not apply action potential extraction algorithms in developing this method. Previous two-photon recordings of GECI-labeled thalamocortical axons projecting from the dorsolateral geniculate nucleus (dLGN) to the primary visual cortex (V1) detected axonal fluorescence transients and suggested that axonal tuning properties to visual stimuli varied as a function of the different V1 layers.[21] The development of an axon-targeting GECI, in which the GAP43 targeting motif was fused into the previously published GCaMP6s GECI to generate the GCaMP6s-axon construct,[13,18] has been shown to increase the intra-axonal GECI concentration and enhance the axonal recording signal-to-noise ratio.[18] Thus, we reasoned that nonlinear microscopy of axonal functionality after TBI could overcome some of the limitations of traditional histological methods by generating data on pathology progression in the same animals over time. We applied this approach to identify that TBI affects the activity patterns of thalamocortical axons in the mouse visual system, and we suggest that this modulation may lead to changes in visual signal processing.

RESULTS

Monitoring axonal activity before and after multimodal TBI

All mice were injected with adeno-associated virus (AAV) solution carrying the GCaMP6s-axon GECI sequence[13,18] into the dLGN. Weekly recording sessions were initiated 4 weeks later in mice that were lightly anesthetized, as conducted previously to characterize functional responses of primary visual cortex neurons.[13,16,17,26–28] Functional activity of dLGN axonal projections in Layer I of V1 was monitored before and after TBI (Figures 1A and 1B), when a multi-directional drifting grating movie was presented to the contralateral eye.[21,29] In this TBI model, an overpressure chamber delivers global concussion, acceleration/deceleration injury, and early blast wave exposure in an isolated manner to the head of an anesthetized mouse. This generates a reproducible pattern of axonal degeneration, cognitive impairment, blood-brain barrier disruption, systemic metabolic alterations, and blood biomarkers that reliably mimic human TBI.[30] Following 2–3 baseline (pre-TBI) axonal activity recordings, mice were randomly assigned to 2 groups (3 mice/group): (1) TBI and (2) sham injury (control), in which mice were subjected to the same procedure except that the overpressure chamber was not activated. Post-TBI and sham injury recordings were conducted once per week over 7 weeks for all groups, starting 3 days after TBI or sham injury (Figure S1A).

Changes in axonal activity patterns following TBI

We detected hundreds of axonal segments within each 200 × 200 μm^2 field of view (FOV; median of 617 segments/FOV, range 240–1159, total number of 268 recordings from 41 FOVs in 6 mice that were segmented using Suite2P[23]; Figure 1C). Individual segments exhibited orientation- and direction-tuned activity when the drifting grating stimulation was presented to the contralateral eye (Figure 1D, see STAR Methods). Response amplitude and additional properties, such as the fraction of segments tuned to the stimulus appearance or to the grating movement in a specific orientation, were substantially increased between the last weekly recording before TBI and the first recording after TBI, with significant interactions of group and time ($p < 0.0001$, 0.0017, and 0.0033, respectively, F-test). The model-estimated mean fractions of axonal segments, which were significantly tuned to the stimulus and exhibited significant orientation selectivity (see STAR Methods for details), increased by 74% and 104%, respectively, for the TBI group (Figures 1E and S1B–S1E and Video S1). The response amplitudes in the TBI group were also increased from a model-estimated mean (95% CI) of 20.7% pre-TBI (12.5%, 31.0%) to 34.6% (23.6%, 47.7%) after TBI, and there was no significant change in the control sham injury group (Figure 1F). Thus, TBI caused significant short-term increases in axonal activity and tuning properties to visual stimuli.

Over the 7 weeks following TBI, the fraction of axonal segments with orientation preference showed significant group-by-time interactions ($p = 0.015$, F-test). Axonal activity properties of the TBI group remained above pre-TBI levels during the entire recording period, with increases in the model-estimated mean of 100%, 70%, and 98% on weeks 1–2, 3–4, and 5–7, respectively (adjusted $p < 0.05$ for these within-group time differences; Figure 2A). The control sham injury group showed smaller changes compared with the baseline values. Comparing the two experimental groups across different time points showed no significant change (Holm-adjusted $p > 0.05$ for all of these within-group comparisons), highlighting the increased statistical power of same-subject, longitudinal monitoring (Figure 2A). The fraction of tuned segments showed a similar, but non-significant, increase as the oriented segments ($p = 0.092$, F-test; Figure S1F) and the ratio of oriented-to-tuned segments gradually increased with a significant group-by-time interaction ($p = 0.0152$, F-test). This ratio increased significantly in TBI mice from a model-estimated mean value of 46.4% pre-TBI to 63.8% and 65.6% in weeks 3–4 and 5–7, respectively, while control sham injury group values remained between 44% and 52% (Figure 2B). Comparing the differences between the two groups across specific time points did not yield any significant changes (adjusted $p > 0.05$ for all comparisons). A significant group-by-time interaction

CellPress
OPEN ACCESS

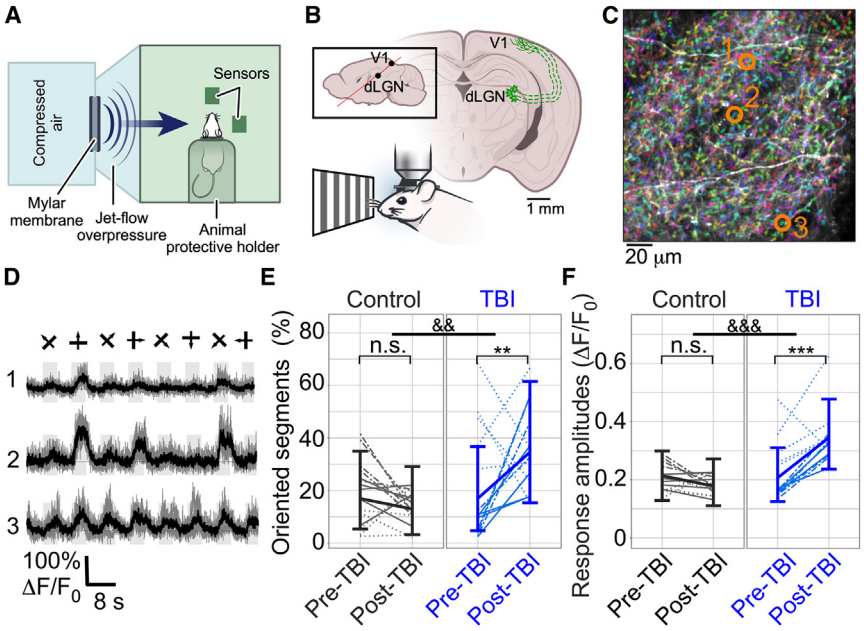

Figure 1. Multimodal TBI causes short-term changes in axonal properties

(A) Schematic of the overpressure chamber used to produce multimodal TBI in mice.

(B) Illustration of the experimental setup. Mice were injected with GCaMP6s-axon into their dLGN, and axonal activity from Layer I of V1 was recorded during the presentation of a drifting grating movie, both before and after TBI.

(C) Example image of axons labeled with GCaMP6s-axon (white over black background) overlaid with the segmentation from Suite2P (arbitrary colors to enhance the contrast of individual segments).

(D) Fluorescence traces of 3 example segments (indicated by orange circles in C). Single trials (gray) and averages of five trials (black) are overlaid. 8 grating motion directions are indicated by arrows as shown above the traces.

(E) The model-estimated mean fraction of axonal segments with significant orientation preference (identified by ANOVA with $p < 0.01$ for each segment's response to the visual stimulation; individual segment data not shown, see STAR Methods for details) was increased from 16.9% to 34.5% for the TBI group between the last weekly recording before injury and the first recording 3–5 days following the injury. This fraction remained similar in the sham control group (gray; $p = 0.003$, F-test, for group-by-time interactions; post-hoc time comparisons within each experimental group found a significant increase in the TBI group with Holm-adjusted $p = 0.003$ but not for the sham control group). &&, $p < 0.01$ for group-by-time interaction; **, $p < 0.01$ for within-group changes; n.s., not significant.

(F) Fluorescence response amplitudes to visual stimulation showed a significant group-by-time interaction ($p < 0.0001$, F-test) with a significant increase in the model-estimated mean for the TBI group of 67% from their pre-TBI levels (Holm-adjusted $p < 0.0001$), while the control group showed no significant changes (same FOVs as in E; &&&, $p < 0.001$ for group-by-time interaction; ***, $p < 0.001$ for within-group changes; n.s., not significant). Within each experimental group, different lines (solid, dotted, and dashed-dotted) show median data from different mice. The thick, solid lines connect the model-estimated mean values, and the error bars show the model-estimated 95% confidence intervals. Figures and models each include 59 measures of 31 FOVs in 6 mice (3 per experimental group).

was identified in the axonal response amplitudes ($p < 0.0001$, F-test), with response amplitudes in the TBI group significantly increased throughout the recording period, while sham control group values stayed similar to baseline (Figure 2C, adjusted $p < 0.01$ for comparing pre-TBI to weeks 1–2, 3–4, and 5–7). Interestingly, most of the increased response amplitudes for the TBI group occurred within the first 2 weeks after injury and remained elevated thereafter (Figure 2C). We also found a non-significant reduction of 15.2% in the model-estimated mean number of detectable axonal segments across all post-TBI weekly recorded FOVs in the TBI group, which is in line with reported axonal degeneration in this injury model[3] ($p = 0.108$, F-test; Figure S1G). These findings demonstrate a substantial change in axonal activity patterns following TBI, which may affect visual input processing in the mouse thalamus and cortex and may also be related to reported behavioral deficits in TBI mice.[3,31–35]

The ability of this method to detect subject-specific effects of TBI on neuronal circuitry was demonstrated by monitoring individual mice within the experimental groups. For example, while all TBI mice exhibited enhanced axonal response amplitudes in the first post-TBI week, 1 mouse in this group also showed subsequent reduced response amplitudes and tuning metrics over the following weeks, whereas the other 2 mice showed increased response amplitudes and tuning (Figure S2). Taken together, our results show that *in vivo* monitoring of axonal tuning after TBI provides a real-time indicator of axonal degeneration and post-TBI pathologic changes to neuronal circuitry.

Changes in single-axon visual acuity over time

As another physiologic functional measure, we also assessed single-axon visual acuity by calculating both the direction sensitivity index (DSI) and orientation sensitivity index (OSI) for individual tuned segments[21,29] (Figures 2D and 2E; see STAR Methods). We identified a significant decrease in DSI ($p < 0.0001$, F-test) and a significant increase in OSI for both groups over time ($p = 0.0289$, F-test). For the control sham injury group, we observed an ~30% longitudinal decrease in model-estimated mean DSI and an ~14% increase in OSI during the recording period, which may be related to physiological changes in the visual system during developmental maturation.[36] For both DSI and OSI, there were no significant interactions between time and experimental group ($p = 0.54$ and $p = 0.52$, respectively). The TBI group exhibited similar trends to the sham control group. Since both groups showed modulated visual acuity over time without a significant difference, the effects of TBI-related deficits on single-axon visual acuity indices could not be determined.

DISCUSSION

Here, we report a method of 2-photon microscopy of axonal-targeting GECIs for *in vivo* monitoring of axonal integrity that enables longitudinal quantification of TBI-induced acute and chronic axonal damage. This method allows repeated measurements from the same brain region within the same mouse over an extended period of time and thereby may assist in reducing the

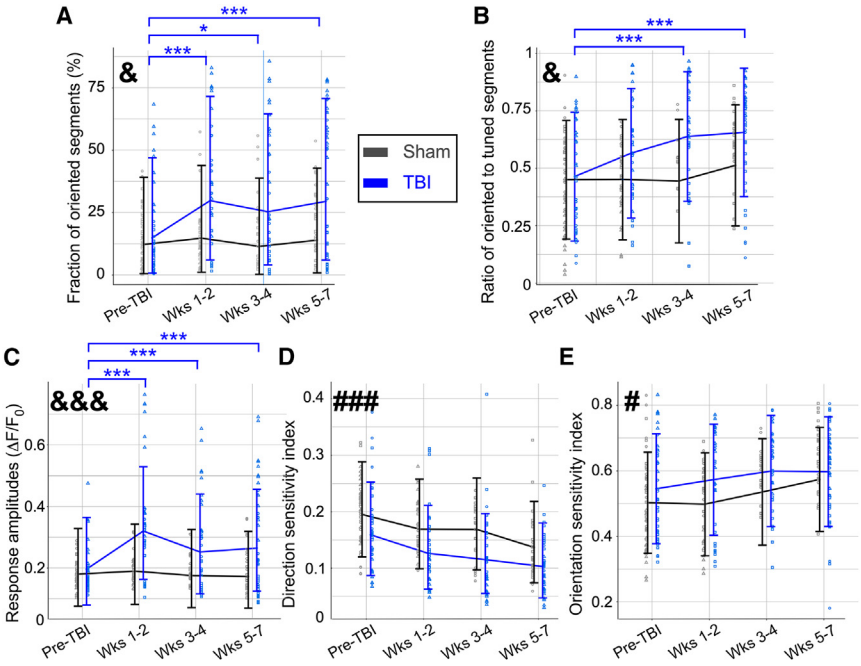

Figure 2. Multimodal TBI causes long-term deficits to thalamocortical axonal activity patterns and tuning to visual stimulation

(A) The fraction of oriented segments showed a significant group-by-time interaction ($p = 0.015$, F-test) with a significant increase in the fraction of oriented segments observed in all post-TBI over pre-TBI for the TBI group (Holm-adjusted $p < 0.05$ in post-hoc comparisons of time within experimental group) but not for the sham control group (Holm-adjusted $p > 0.05$ for all paired time comparisons). &, $p < 0.05$ for group-by-time interaction; *, $p < 0.05$ for TBI within-group time differences; ***, $p < 0.001$ for TBI within-group time differences.

(B) The ratio of oriented-to-tuned segments showed a significant group-by-time interaction ($p = 0.015$, F-test) with a significant increase in the measured ratio for the TBI group after TBI (Holm-adjusted $p < 0.001$ and $p < 0.0001$ for pre-TBI vs. weeks 3–4 and 5–7, respectively) but no significant changes for the sham control group (Holm-adjusted $p > 0.05$ for all time comparisons).

(C) The measured fluorescence response amplitudes for a drifting grating simulation showed a group-by-time interaction ($p < 0.0001$, F-test), and model-estimated mean amplitudes were 63% higher in TBI mice in the first 1–2 weeks after TBI compared with the pre-TBI period (Holm-adjusted $p < 0.0001$). Response amplitudes remained higher by 29% and 35% on weeks 3–4 and 5–7, respectively (Holm-adjusted $p < 0.01$ and $p < 0.001$ respectively). The sham control group did not show such an increase, and there was no significant difference in time effects between them (Holm-adjusted $p > 0.05$ for all time comparisons).

(D) The median DSI value of the tuned segments showed a significant decrease over time for both groups ($p < 0.0001$, F-test) but without a group-by-time interaction ($p = 0.541$, F-test). ###, $p < 0.001$ for time effect.

(E) The median OSI value of the tuned segments showed a significant increase over time for both groups ($p = 0.029$, F-test) but without a group-by-time interaction ($p = 0.522$, F-test; same FOVs as in C). Within each group, median data from individual mice are represented by different markers (square, triangle, circle). The lines connect the model-estimated marginal mean values, and the error bars show the model-estimated 95% confidence intervals. Figures and models each include 268 measures of 41 FOVs in 6 mice (3 per experimental group).

number of animals needed for large longitudinal preclinical studies. The potential reduction of sample size, which aligns with the current literature,[10,11,37] can be demonstrated by simulating a power calculation to determine required mouse numbers when comparing 2 groups with a large group-by-time interaction effect (partial eta squared = 0.25) occurring in 2 groups measured at 4 times with a correlation of 0.5. This shows that detecting significant differences (adjusted $p < 0.05$) across groups using measurements from the same subjects could be detected with 80% power with a total of 6 subjects (n = 3 mice/group). By contrast, detecting the same interaction partial eta squared in a 2-way ANOVA in which different subjects are measured at each of 4 time points would require a total of 40 subjects (n = 5 mice/group sacrificed at each time point) to achieve the same power. These results align with the group size used in this study, as well as the group size previously used to identify axonal degeneration using standard histological processing.[3] Additional advantages of the presented method are extraction of the functional activity patterns of axonal response to visual stimuli to assess some of the mouse visual system properties, monitoring of changes in specific axons and brain regions, and acquisition of data on longitudinal changes in the recovery patterns of specific animals.

We found that TBI-induced axonal pathology was detected within days after injury and did not return to baseline during the chronic recording period of 7 weeks. This finding aligns with the known long-term effects of TBI.[32] Our method also allows *in vivo* identification of variability across animals (Figure S2), and future work may compare this variability with behavioral deficits, such as impaired visual acuity. However, we note that comprehensive description of variability across mice after TBI will require testing a larger cohort size. Here, we limited our scope to the proof of principle of this method. Depending upon the injury, disease paradigm, and expected effect size, application of this technique will require different numbers of mice to achieve appropriate statistical power.

We also note that 2-photon microscopy monitoring of GECI signal provides additional advantages, which may be combined with the presented method. For example, selective labeling of genetically defined cellular populations, such as sub-types of excitatory or inhibitory neurons,[38,39] may enable studying potential differences in activity patterns across these populations during recovery. In addition, applying dual-color GECI labeling[28,40,41] to target different cellular populations or components, such as axons and somata, may enable investigation of how the modified axonal activity patterns we identified translates to somatic functional activity of V1 neurons.

In conclusion, axonal degeneration plays a central role in multiple neurodegenerative conditions, and the small size and large distribution of axons across multiple brain regions makes

it challenging to apply conventional tissue histological processing to large preclinical studies. Moreover, postmortem histology precludes monitoring of trends of recovery or degeneration of axons within the same animal. Repeated measurements of axonal function within the same animal reduce the complication of between-animal variability[9] that is otherwise inevitable when using postmortem axonal assessment methods that require sacrifice of multiple animals at various time points. Moreover, applying statistical methods that incorporate same-subject, longitudinal, and hierarchical data to increase statistical power, such as the linear mixed-model effects analysis used in this study (see STAR Methods for details), may facilitate more efficient identification of different recovery patterns across the studied subjects following TBI.[42] Therefore, the presented method will assist in reducing the required number of animals for monitoring axonal degeneration after TBI, which will facilitate more efficient testing of new treatments. Notably, axonal degeneration is an integral aspect of both normal aging as well as most neurodegenerative conditions, including AD, PD, and amyotrophic lateral sclerosis.[43] Thus, this approach can be similarly applied to monitor axonal degeneration in other preclinical models of injury or neurodegeneration to investigate pathology and evaluate putative neuroprotective treatments for these conditions.

Limitations of the study

Functional recording from axons is limited to a sub-population of axons that survive TBI. Once axons die, activity cannot be recorded. In addition, longitudinal monitoring of AAV-driven GECI signal is limited to several months, as previous reports show a gradual increase in intracellular GECI concentration over the course of weeks, which eventually leads to cell death.[13,44]

STAR★METHODS

Detailed methods are provided in the online version of this paper and include the following:

- KEY RESOURCES TABLE
- RESOURCE AVAILABILITY
  - Lead contact
  - Materials availability
  - Data and code availability
- EXPERIMENTAL MODEL AND SUBJECT DETAILS
  - Animals
- METHOD DETAILS
  - Craniotomy surgeries and injection of viral particles
  - Recording of axonal activity
  - Multimodal TBI
- QUANTIFICATION AND STATISTICAL ANALYSIS
  - Data analyses
  - Statistical analyses

SUPPLEMENTAL INFORMATION

Supplemental information can be found online at https://doi.org/10.1016/j.crmeth.2023.100481.

ACKNOWLEDGMENTS

We thank Drs. Christopher Nelson and Dimitrios Davalos for reading and commenting on the content of this manuscript. We thank the HHMI Janelia GENIE project for sharing the GCaMP6s GECI, and Dr. Lin Tian's lab for sharing the GCaMP6s-axon construct. We thank Drs. Harris, Carandini, Pachitariu, and their colleagues for sharing the Suite2P analysis platform. The graphical abstract was made with Biorender. H.D. and A.A.P. were supported by a Cleveland Brain Health Initiative Scholars Award. A.A.P. was additionally generously supported for this work by Karen and David Crane, and as the Case Western Reserve University Rebecca E. Barchas, M.D., Professor in Translational Psychiatry, the University Hospitals Morley-Mather Chair in Neuropsychiatry, and by Project 19PABH134580006-AHA/Allen Initiative in Brain Health and Cognitive Impairment. A.A.P. also acknowledges support from the Brockman Foundation, the Department of Veterans Affairs Merit Award I01BX005976, NIH/NIGMS RM1 GM142002, NIH/NIA RO1AG066707, NIH/NIA 1 U01 AG073323, the Elizabeth Ring Mather & William Gwinn Mather Fund, S. Livingston Samuel Mather Trust, G.R. Lincoln Family Foundation, Waitt Foundation, Gordon and Evie Safran, the Leonard Krieger Fund of the Cleveland Foundation, the Maxine and Lester Stoller Parkinson's Research Fund, the Louis Stokes VA Medical Center resources and facilities, and the Translational Therapeutics Core of the Cleveland Alzheimer's Disease Research Center (NIH/NIA 1 P30 AGO62428-01). M.-K.S. was supported by the BrightFocus Foundation (A2019551F). E.M. was supported by the Alzheimer's Disease Translational Data Science Training Program NIH T32 AG071474. E.V.-R. was supported by Department of Defense Peer-Reviewed Alzheimer's Research Program (PRARP) Award AZ210092 (W81XWH-22-1-0129).

AUTHOR CONTRIBUTIONS

The work was conceived by H.D. and A.A.P. S.C. performed the surgical procedures and functional imaging recordings, and the data were analyzed by J.A.B., D.P., and H.D. TBI experiments and graphical abstract preparation were done by M.-K.S., E.M., and E.V.-R. Statistical analysis was performed by B.W. The manuscript was written by H.D., B.W., and A.A.P., with comments from other authors.

DECLARATION OF INTERESTS

None of the authors have any competing interests.

INCLUSION AND DIVERSITY

One or more of the authors of this paper self-identifies as an underrepresented ethnic minority in their field of research or within their geographical location. One or more of the authors of this paper self-identifies as a gender minority in their field of research. One or more of the authors of this paper self-identifies as living with a disability.

Received: November 25, 2022
Revised: March 30, 2023
Accepted: April 21, 2023
Published: May 16, 2023

REFERENCES

1. Maas, A.I.R., Menon, D.K., Adelson, P.D., Andelic, N., Bell, M.J., Belli, A., Bragge, P., Brazinova, A., Büki, A., Chesnut, R.M., et al. (2017). Traumatic brain injury: integrated approaches to improve prevention, clinical care, and research. Lancet Neurol. *16*, 987–1048.
2. Ma, V.Y., Chan, L., and Carruthers, K.J. (2014). Incidence, prevalence, costs, and impact on disability of common conditions requiring rehabilitation in the United States: stroke, spinal cord injury, traumatic brain injury, multiple sclerosis, osteoarthritis, rheumatoid arthritis, limb loss, and back pain. Arch. Phys. Med. Rehabil. *95*, 986–995.e1.

3. Yin, T.C., Voorhees, J.R., Genova, R.M., Davis, K.C., Madison, A.M., Britt, J.K., Cintrón-Pérez, C.J., McDaniel, L., Harper, M.M., and Pieper, A.A. (2016). Acute axonal degeneration drives development of cognitive, motor, and visual deficits after blast-mediated traumatic brain injury in mice. Eneuro *3*. ENEURO.0220-16.2016.

4. Johnson, V.E., Stewart, W., and Smith, D.H. (2013). Axonal pathology in traumatic brain injury. Exp. Neurol. *246*, 35–43.

5. Barker S, P.B., and Pieper, A.A. (2023). Increased risk of aging-related neurodegenerative disease after traumatic brain injury. Biomedicines *11*. https://doi.org/10.3390/biomedicines11041154.

6. Jourdan, C., Azouvi, P., Genêt, F., Selly, N., Josseran, L., and Schnitzler, A. (2018). Disability and health consequences of traumatic brain injury: national prevalence. Am. J. Phys. Med. Rehabil. *97*, 323–331.

7. Delic, V., Beck, K.D., Pang, K.C.H., and Citron, B.A. (2020). Biological links between traumatic brain injury and Parkinson's disease. Acta Neuropathol. Commun. *8*, 45.

8. Long, J.M., and Holtzman, D.M. (2019). Alzheimer disease: an update on pathobiology and treatment strategies. Cell *179*, 312–339.

9. Vickers, A.J. (2003). How many repeated measures in repeated measures designs? Statistical issues for comparative trials. BMC Med. Res. Methodol. *3*, 22. https://doi.org/10.1186/1471-2288-3-22.

10. Sullivan, L.M. (2008). Repeated measures. Circulation *117*, 1238–1243. https://doi.org/10.1161/CIRCULATIONAHA.107.654350.

11. Morgan, T.M., and Case, L.D. (2013). Conservative sample size determination for repeated measures analysis of covariance. Ann. Biom. Biostat. *1*, 1002.

12. Huber, D., Gutnisky, D.A., Peron, S., O'Connor, D.H., Wiegert, J.S., Tian, L., Oertner, T.G., Looger, L.L., and Svoboda, K. (2012). Multiple dynamic representations in the motor cortex during sensorimotor learning. Nature *484*, 473–478.

13. Chen, T.W., Wardill, T.J., Sun, Y., Pulver, S.R., Renninger, S.L., Baohan, A., Schreiter, E.R., Kerr, R.A., Orger, M.B., Jayaraman, V., et al. (2013). Ultrasensitive fluorescent proteins for imaging neuronal activity. Nature *499*, 295–300.

14. Das, A., Bastian, C., Trestan, L., Suh, J., Dey, T., Trapp, B.D., Baltan, S., and Dana, H. (2019). Reversible loss of hippocampal function in a mouse model of demyelination/remyelination. Front. Cell. Neurosci. *13*, 588.

15. Dana, H., and Shoham, S. (2020). Two-photon microscopy in the mammalian brain. In Handbook of Neurophotonics (CRC Press), pp. 55–80.

16. Chornyy, S., Das, A., Borovicka, J.A., Patel, D., Chan, H.H., Hermann, J.K., Jaramillo, T.C., Machado, A.G., Baker, K.B., and Dana, H. (2021). Cellular-resolution monitoring of ischemic stroke pathologies in the rat cortex. Biomed. Opt. Express *12*, 4901–4919.

17. Dana, H., Sun, Y., Mohar, B., Hulse, B.K., Kerlin, A.M., Hasseman, J.P., Tsegaye, G., Tsang, A., Wong, A., Patel, R., et al. (2019). High-performance calcium sensors for imaging activity in neuronal populations and microcompartments. Nat. Methods *16*, 649–657.

18. Broussard, G.J., Liang, Y., Fridman, M., Unger, E.K., Meng, G., Xiao, X., Ji, N., Petreanu, L., and Tian, L. (2018). In vivo measurement of afferent activity with axon-specific calcium imaging. Nat. Neurosci. *21*, 1272–1280.

19. Zhang, Y., Rózsa, M., Liang, Y., Bushey, D., Wei, Z., Zheng, J., Reep, D., Broussard, G.J., Tsang, A., Tsegaye, G., et al. (2023). Fast and sensitive GCaMP calcium indicators for imaging neural populations. Nature *615*, 884–891. https://doi.org/10.1038/s41586-023-05828-9.

20. Kerlin, A., Mohar, B., Flickinger, D., MacLennan, B.J., Dean, M.B., Davis, C., Spruston, N., and Svoboda, K. (2019). Functional clustering of dendritic activity during decision-making. Elife *8*, e46966.

21. Sun, W., Tan, Z., Mensh, B.D., and Ji, N. (2016). Thalamus provides layer 4 of primary visual cortex with orientation- and direction-tuned inputs. Nat. Neurosci. *19*, 308–315. https://doi.org/10.1038/nn.4196.

22. Deneux, T., Kaszas, A., Szalay, G., Katona, G., Lakner, T., Grinvald, A., Rózsa, B., and Vanzetta, I. (2016). Accurate spike estimation from noisy calcium signals for ultrafast three-dimensional imaging of large neuronal populations in vivo. Nat. Commun. *7*, 12190.

23. Pachitariu, M., Stringer, C., Dipoppa, M., Schröder, S., Rossi, L.F., Dalgleish, H., Carandini, M., and Harris, K.D. (2017). Suite2p: beyond 10,000 neurons with standard two-photon microscopy. Preprint at bioRxiv. https://doi.org/10.1101/061507.

24. Pnevmatikakis, E.A., Soudry, D., Gao, Y., Machado, T.A., Merel, J., Pfau, D., Reardon, T., Mu, Y., Lacefield, C., Yang, W., et al. (2016). Simultaneous denoising, deconvolution, and demixing of calcium imaging data. Neuron *89*, 285–299. https://doi.org/10.1016/j.neuron.2015.11.037.

25. Friedrich, J., Zhou, P., and Paninski, L. (2017). Fast online deconvolution of calcium imaging data. PLoS Comput. Biol. *13*, e1005423. https://doi.org/10.1371/journal.pcbi.1005423.

26. Akerboom, J., Chen, T.W., Wardill, T.J., Tian, L., Marvin, J.S., Mutlu, S., Calderón, N.C., Esposti, F., Borghuis, B.G., Sun, X.R., et al. (2012). Optimization of a GCaMP calcium indicator for neural activity imaging. J. Neurosci. *32*, 13819–13840.

27. Dana, H., Novak, O., Guardado-Montesino, M., Fransen, J.W., Hu, A., Borghuis, B.G., Guo, C., Kim, D.S., and Svoboda, K. (2018). Thy1 transgenic mice expressing the red fluorescent calcium indicator jRGECO1a for neuronal population imaging in vivo. PLoS One *13*, e0205444.

28. Dana, H., Mohar, B., Sun, Y., Narayan, S., Gordus, A., Hasseman, J.P., Tsegaye, G., Holt, G.T., Hu, A., Walpita, D., et al. (2016). Sensitive red protein calcium indicators for imaging neural activity. Elife *5*, e12727.

29. Niell, C.M., and Stryker, M.P. (2008). Highly selective receptive fields in mouse visual cortex. J. Neurosci. *28*, 7520–7536.

30. Shin, M.-K., Vázquez-Rosa, E., Cintrón-Pérez, C.J., Riegel, W.A., Harper, M.M., Ritzel, D., and Pieper, A.A. (2021). Characterization of the jet-flow overpressure model of traumatic brain injury in mice. Neurotrauma Rep. *2*, 1–13.

31. Shin, M.K., Vázquez-Rosa, E., Koh, Y., Dhar, M., Chaubey, K., Cintrón-Pérez, C.J., Barker, S., Miller, E., Franke, K., Noterman, M.F., et al. (2021). Reducing acetylated tau is neuroprotective in brain injury. Cell *184*, 2715–2732.e23. https://doi.org/10.1016/j.cell.2021.03.032.

32. Vázquez-Rosa, E., Shin, M.K., Dhar, M., Chaubey, K., Cintrón-Pérez, C.J., Tang, X., Liao, X., Miller, E., Koh, Y., Barker, S., et al. (2020). P7C3-A20 treatment one year after TBI in mice repairs the blood-brain barrier, arrests chronic neurodegeneration, and restores cognition. Proc. Natl. Acad. Sci. USA *117*, 27667–27675. https://doi.org/10.1073/pnas.2010430117.

33. Vázquez-Rosa, E., Watson, M.R., Sahn, J.J., Hodges, T.R., Schroeder, R.E., Cintrón-Pérez, C.J., Shin, M.K., Yin, T.C., Emery, J.L., Martin, S.F., et al. (2019). Neuroprotective efficacy of a Sigma 2 receptor/TMEM97 modulator (DKR-1677) after traumatic brain injury. ACS Chem. Neurosci. *10*, 1595–1602. https://doi.org/10.1021/acschemneuro.8b00543.

34. Yin, T.C., Britt, J.K., De Jesús-Cortés, H., Lu, Y., Genova, R.M., Khan, M.Z., Voorhees, J.R., Shao, J., Katzman, A.C., Huntington, P.J., et al. (2014). P7C3 neuroprotective chemicals block axonal degeneration and preserve function after traumatic brain injury. Cell Rep. *8*, 1731–1740. https://doi.org/10.1016/j.celrep.2014.08.030.

35. Dutca, L.M., Stasheff, S.F., Hedberg-Buenz, A., Rudd, D.S., Batra, N., Blodi, F.R., Yorek, M.S., Yin, T., Shankar, M., Herlein, J.A., et al. (2014). Early detection of subclinical visual damage after blast-mediated TBI enables prevention of chronic visual deficit by treatment with P7C3-S243. Invest. Ophthalmol. Vis. Sci. *55*, 8330–8341.

36. Wong, A.A., and Brown, R.E. (2007). Age-related changes in visual acuity, learning and memory in C57BL/6J and DBA/2J mice. Neurobiol. Aging *28*, 1577–1593.

37. Mowinckel, P., Hagen, K.B., Heiberg, T., and Kvien, T.K. (2008). Repeated measures in rheumatoid arthritis reduced the required sample size in a two-armed clinical trial. J. Clin. Epidemiol. *61*, 940–944. https://doi.org/10.1016/j.jclinepi.2007.12.004.

38. Groblewski, P.A., Ollerenshaw, D.R., Kiggins, J.T., Garrett, M.E., Mochizuki, C., Casal, L., Cross, S., Mace, K., Swapp, J., Manavi, S., et al.

(2020). Characterization of learning, motivation, and visual perception in five transgenic mouse lines expressing GCaMP in distinct cell populations. Front. Behav. Neurosci. *14*, 104. https://doi.org/10.3389/fnbeh.2020.00104.

39. Daigle, T.L., Madisen, L., Hage, T.A., Valley, M.T., Knoblich, U., Larsen, R.S., Takeno, M.M., Huang, L., Gu, H., Larsen, R., et al. (2018). A suite of transgenic driver and reporter mouse lines with enhanced brain-cell-type targeting and functionality. Cell *174*, 465–480.e22. https://doi.org/10.1016/j.cell.2018.06.035.
40. Inoue, M., Takeuchi, A., Manita, S., Horigane, S.-i., Sakamoto, M., Kawakami, R., Yamaguchi, K., Otomo, K., Yokoyama, H., Kim, R., et al. (2019). Rational engineering of XCaMPs, a multicolor GECI suite for in vivo imaging of complex brain circuit dynamics. Cell *177*, 1346–1360.e24. https://doi.org/10.1016/j.cell.2019.04.007.
41. Inoue, M., Takeuchi, A., Horigane, S.-i., Ohkura, M., Gengyo-Ando, K., Fujii, H., Kamijo, S., Takemoto-Kimura, S., Kano, M., Nakai, J., et al. (2015). Rational design of a high-affinity, fast, red calcium indicator R-CaMP2. Nat. Methods *12*, 64–70.
42. Davis, C.S. (2002). Statistical Methods for the Analysis of Repeated Measurements (Springer).
43. Salvadores, N., Sanhueza, M., Manque, P., and Court, F.A. (2017). Axonal degeneration during aging and its functional role in neurodegenerative disorders. Front. Neurosci. *11*, 451.
44. Tian, L., Hires, S.A., Mao, T., Huber, D., Chiappe, M.E., Chalasani, S.H., Petreanu, L., Akerboom, J., McKinney, S.A., Schreiter, E.R., et al. (2009). Imaging neural activity in worms, flies and mice with improved GCaMP calcium indicators. Nat. Methods *6*, 875–881. https://doi.org/10.1038/nmeth.1398.
45. Brainard, D.H. (1997). The psychophysics toolbox. Spat. Vis. *10*, 433–436.
46. Pelli, D.G. (1997). The VideoToolbox software for visual psychophysics: transforming numbers into movies. Spat. Vis. *10*, 437–442.
47. Thévenaz, P., Ruttimann, U.E., and Unser, M. (1998). A pyramid approach to subpixel registration based on intensity. IEEE Trans. Image Process. *7*, 27–41.
48. Tango, T. (2016). On the repeated measures designs and sample sizes for randomized controlled trials. Biostatistics *17*, 334–349.
49. Detry, M.A., and Ma, Y. (2016). Analyzing repeated measurements using mixed models. JAMA *315*, 407–408.
50. R Core Team (2022). R: A Language and Environment for Statistical Computing (R Foundation for Statistical Computing).
51. Pinheiro, J., Bates, D., DebRoy, S., and Sarkar, D.; R Core Team (2022). Nlme: Linear and Nonlinear Mixed Effects Models, pp. 1–155. R package version 3.
52. Russell, L. (2022). Emmeans: Estimated Marginal Means, Aka Least-Squares Means. R package version 1.7.3.
53. Faul, F., Erdfelder, E., Lang, A.-G., and Buchner, A. (2007). G* Power 3: a flexible statistical power analysis program for the social, behavioral, and biomedical sciences. Behav. Res. Methods *39*, 175–191.

STAR★METHODS

KEY RESOURCES TABLE

REAGENT or RESOURCE	SOURCE	IDENTIFIER
Bacterial and virus strains		
AAV1-hSynapsin1-axon-GCaMP6s.	Addgene	Cat#111262-AAV1
Experimental models: Organisms/strains		
C57Bl/6J mice	Jackson Laboratories	Cat#000664
Recombinant DNA		
GCaMP6s-axon (Genetically-Encoded Calcium Indicator)	Broussard et al.[18]	https://doi.org/10.1038/s41593-018-0211-4
Software and algorithms		
MATLAB	Mathworks	R2021b
Suite2P	Pachitariu et al.[23]	https://doi.org/10.1101/061507 https://github.com/MouseLand/suite2p
ThorImage	Thorlabs	Version 4.0
R	The R Project for Statistical Computing	https://www.r-project.org/
Photoshop	Adobe	https://www.adobe.com/products/photoshop.html
Canvas X Draw	Canvas GFX	https://www.canvasgfx.com/products/canvas-x-draw
MATLAB scripts	Mathworks	Methods S1
Other		
TBI-induction device	Custom-made	https://doi.org/10.1089/neur.2020.0020
Two-photon microscope	Thorlabs	Bergamo II

RESOURCE AVAILABILITY

Lead contact

Further information and requests for resources and reagents should be directed to and will be fulfilled by the lead contact, Hod Dana (danah@ccf.org).

Materials availability

This study did not generate new unique reagents.

Data and code availability

- The data that support the findings of this study are available from the corresponding authors upon reasonable request.
- All original code generated in this study is included in this paper's supplemental information.
- Any additional information required to reanalyze the data reported in this paper is available from the lead contact upon request.

EXPERIMENTAL MODEL AND SUBJECT DETAILS

Animals

All surgical and experimental procedures were conducted in accordance with protocols approved by the Institutional Animal Care and Use Committee and Institutional Biosafety Committee of the Cleveland Clinic Lerner Research Institute, as well as the Louis Stokes Cleveland Veterans Affairs Medical Center Institutional Animal Care and Use Committee. C57BL/6J mice (6 mice, 2 females and 4 males, 3.5 months old at the beginning of the study; Jackson Laboratories strain #000664) were group-housed in standard vivarium conditions until the start of the study. The vivarium was maintained at 20–21°C and food (Teklad 2918 regular diet, Envigo) and water were available *ad libitum.* Lights were kept on a 12-h light/12-h dark cycle, and experiments were conducted during the light time.

CellPress
OPEN ACCESS

METHOD DETAILS

Craniotomy surgeries and injection of viral particles

Six C57BL/6J mice (4 males and 2 females, 3.5 months of age) were anesthetized using isoflurane (3% for induction, 1.5% during the surgery), placed on a heating pad, and then injected with local analgesic (0.5% Bupivacaine) and pain (Buprenorphine, 0.2 mg/kg) medications followed by exposure of the skull bone above the left hemisphere. A 3 × 5 mm^2 craniotomy was drilled above the left cortex (covering the area from bregma to Lambda and midline+0.5mm to 3.5 mm laterally), the bone was gently removed, and 60 nL solution of adeno-associated virus 1 (AAV1) expressing the GCaMP6s-axon GECI under the human synapsin1 promoter (SYN1; Addgene catalog number 111262-AAV1) was injected into the dLGN (9 injection spots per mouse at the following coordinates[21]: −1.8mm/-2.2mm (AP/LV), −2.2mm/-2.2mm, and −2.4mm/-2.2mm; injection depths were 2.7mm, 3mm, and 3.3mm). All injections were done using pulled and beveled 1mm glass micropipettes (Sutter Borosilicate glass micropipettes without filament, B100-50-10; Sutter P-1000 and BV-10, for pulling and beveling, respectively) and a syringe pump (UMP3T-1, World Precision Instruments) at a rate of 60 nL/min. The craniotomy was covered with a custom-made glass window (Tower Optical Corporation) and cemented to the bone using dental cement (Contemporary ortho-Jet, Lang Dental). A custom-made stainless steel head bar was attached to the skull. Mice were given post-operative care (Ketoprofen 5 mg/kg) and 4 weeks for recovery and to allow for sufficient GECI expression.

Recording of axonal activity

Axonal activity recording was performed using a two-photon microscope with galvo-resonant scanners and GaAsP PMT detectors (Bergamo II, Thorlabs) at 950 nm excitation wavelength (Insight X3, Spectra-Physics) using a 16x, 0.8 NA objective (MRP07220, Nikon). Mice were lightly-anesthetized (0.5% isoflurane), injected with a sedative (Chlorprothixene Hydrochloride, Sigma; intra-muscular injection of 30 μL of 0.33 mg/mL solution), and placed on a heating pad in the dark, as previously reported.[13,17,27,28] Fluorescence data were recorded using the ThorImage software (Thorlabs, version 4.0), which controlled the microscope. Dense axonal labeling in Layer I of V1 was apparent four weeks after AAV injection. Visual stimulation was presented to the right eye, generated using the psychophysical toolbox[45,46] in MATLAB (Mathworks), and synchronized with the recording data using ThorSynch software. An LCD monitor was used for stimulus presentation (30 × 36 cm^2 display, located 15 cm in from of the mouse right eye, tilted 45° with respect to the nose line, and covered with a blue plexiglass to minimize fluorescence signal contamination) that subtended an angle of ±50° horizontally and ±45° vertically. The visual stimulus consisted of black-and-white moving bars (a drifting grating) that appeared on the screen and moved parallelly in 1 of 8 directions (from 0°, which corresponds to the grating moving upward on the screen, to 315°, with 45° increments) for 4 s, which were followed by additional 4 s of gray display to allow the visual-evoked activity and GCaMP6 signal to subside. Then a grating moving in the next movement direction appeared for 4 s, and so on. This stimulation cycle was repeated 5 times. Similar visual stimulation protocols were previously used to elicit solid responses from dLGN axons and V1 neurons.[13,21] FOVs of ∼200 × 200 $μm^2$ with 512 × 512 pixels were recorded at 30Hz. Typically, 5 different FOVs were recorded from each mouse in each recording session. The different FOVs were identified by their location with respect to bregma (using a motorized stage with 1-μm resolution), as well as the shape of the local vasculature, which was apparent in the two-photon microscopy images as black shapes on the gray background of GCaMP6s-axon signal. During subsequent recordings, we returned to the same coordinates and used the local vasculature as a map (See Video S1) to locate the brightest axons within the FOV so that we could then record from the same location. If the exact location of a specific FOV could not be determined due to changes in the brain condition (i.e., degeneration of axons or changes in vasculature shape after TBI), then a nearby location (several hundred microns from the original FOV) was recorded. Over the following weeks, we continued recording from the same modified location. FOVs were excluded from analysis if there were severe movements, or if visual stimulation was not synchronized with recording. All mice were recorded 2–3 times before TBI and then every week for 7 weekly recordings after TBI except for mouse 5, which was removed from the study after 5 weeks of recording due to a medical condition.

Multimodal TBI

Mice were assigned into TBI and sham injury groups (n = 3 mice/group). TBI mice were anesthetized with ketamine/xylazine (100/10 mg/kg) via intraperitoneal injection and placed in an enclosed chamber constructed from an air tank partitioned into two sides and separated by a port covered by a mylar membrane. Pressure in the side not containing the mouse was increased to cause membrane rupture at 20 pounds per square inch (PSI), generating ∼1.0- to 1.5-m/s air jet flow of 137.9 ± 2.09 kPa that passes through the animal's head. The head was untethered in a padded holder while the body was shielded by a metal tube. The jet of air produced upon membrane rupture produces a collimated high-speed jet flow with dynamic pressure that delivers a compressive impulse. Variable rupture dynamics of the diaphragm through which the jet flow originates also generate a weak shock front. There is also a minor component of acceleration–deceleration injury to the unrestrained head. The sham injury (control) group was anesthetized and passed through the same process except for the injury. After several hours of monitoring, mice were returned to regular housing. All mice were included in the study and were randomly assigned to experimental groups and recording days; no experimental blinding was used.

QUANTIFICATION AND STATISTICAL ANALYSIS

Data analyses

Small drifts and movements of the imaged area throughout recording were corrected using TurboReg plug-in of ImageJ.[47] Axonal segmentation was done using Suite2P[23] with experimenter supervision. Remaining analyses were conducted with custom MATLAB scripts. Fluorescence signal was averaged from all pixels within each segment. Neuropil signal was subtracted, as previously done,[13,26] with a coefficient of 0.7. Baseline fluorescence (F_{base}) for each segment was calculated by averaging fluorescence for 0.66 s before visual stimulation. The response amplitude (F_{resp}) was calculated as peak amplitude of fluorescence signal during the drifting grating appearance and calculating:

$$\frac{\Delta F}{F_0} = \frac{F_{resp} - F_{base}}{F_{base}}$$

Detection of tuning of segments to visual stimulus (tuned segments) was calculated similar to previous studies[13,16,17,26] using a one-way ANOVA test ($p = 0.01$) between mean fluorescence signal during stimulus presentation vs. during presentation of gray display. Segments that passed the ANOVA test and had a positive response amplitude larger than 5% were defined as tuned segments. A second one-way ANOVA test ($p = 0.01$) was conducted among the tuned segments between mean fluorescence signal during presentation of each of the 8 directions determined whether these segments had an orientation preference (oriented segment). Orientation sensitivity index (OSI) and direction sensitivity index (DSI) were calculated as previously defined.[26,29] The preferred angle for each tuned segment was determined as the grating angle that elicited the highest fluorescence amplitude change (θ_{pref}). We calculated $OSI = \frac{\theta_{pref} - \theta_{orth}}{\theta_{pref} + \theta_{orth}}$, where $\theta_{orth} = \theta_{pref} + \frac{\pi}{2}$. Similarly, $DSI = \frac{\theta_{pref} - \theta_{opposite}}{\theta_{pref} + \theta_{oppoite}}$, where $\theta_{opposite} = \theta_{pref} + \pi$. MATLAB scripts with the analysis code are attached to the Supplementary Information.

Statistical analyses

For comparing across groups and for the effect of time, we used a linear mixed-model effects approach to model our data.[9,48,49] This model allows analyzing hierarchical data structure with multiple non-independent recordings of FOVs from the same mouse, which are nested in independent recordings across different mice. We grouped data together from 2 to 3 recording sessions (pre-TBI, weeks 1–2, 3–4, and 5–7 post-TBI) to assess the effects of time, experimental group, and their interaction given the repeated measures of FOV and multiple FOVs measured within each mouse, considering FOV within mouse as nested random effects. The significance of the modeled fixed effects of time, experimental group, and their interaction were assessed with F-tests using the marginal sum of squares and considered significant at $p < 0.05$. Model assumptions were assessed for each endpoint and square-root transformations were imposed for percentage of tuned and oriented segments, response amplitude, OSI, and DSI. Model-estimated marginal means and 95% confidence intervals were calculated and overlayed on observed data in figures with distinct line types or symbols for each mouse within a group. Measurements following small location changes in the FOV required across time as described above were considered to be grouped with the measurements from the original FOV location as a measured unit with a random effect. The number of distinct FOVs reported in results and figures reflects this grouping.

When a significant interaction was detected, post-hoc tests were implemented to identify if the experimental groups differed in any of the four time estimates or in which experimental group we observed significant changes over time (pairwise tests of time parameters within experimental group with containment degrees of freedom). Within each model, the p values of all post-hoc tests were adjusted using the Holm method and considered significant at $p < 0.05$. All analyses were performed in R (Version 4.1.3)[50] and included functions from the nlme and emmeans packages.[51,52] Power analyses presented in discussion were calculated using G*Power.[53]

Cell Reports Methods, Volume *3*

Supplemental information

Longitudinal *in vivo* monitoring of axonal degeneration after brain injury

Sergiy Chornyy, Julie A. Borovicka, Davina Patel, Min-Kyoo Shin, Edwin Vázquez-Rosa, Emiko Miller, Brigid Wilson, Andrew A. Pieper, and Hod Dana

Supplementary information

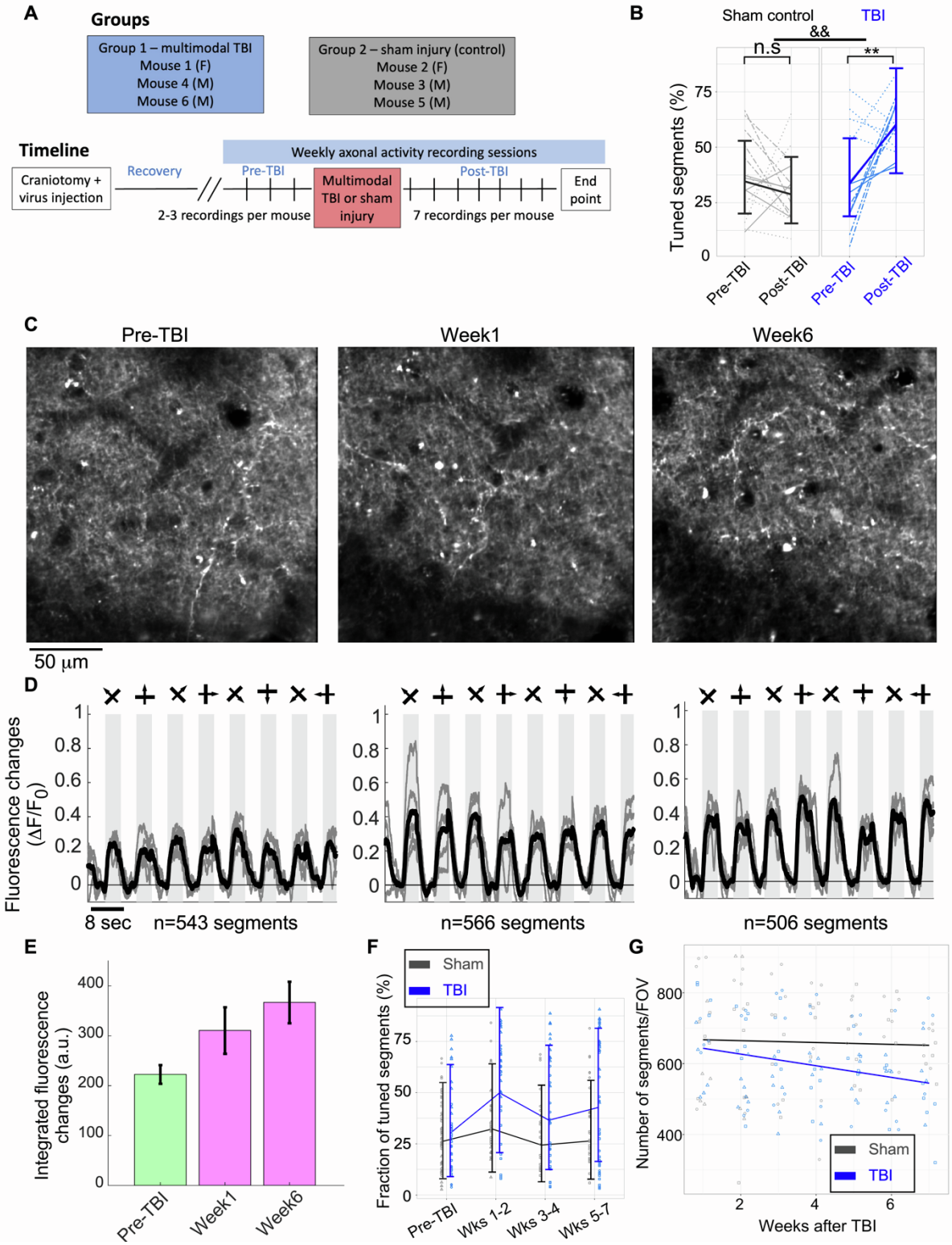

Supplementary Figure 1. Experimental design and additional data related to STAR Methods and Main Figs. 1-2. A. Six male and female mice (M and F, respectively) were randomly divided into 2 groups: TBI and sham injury (control). All mice were implanted with cranial windows and injected with GCaMP6s-axon into their dLGN. We recorded 2-3 sessions of baseline visual stimulated activity before exposing mice in the TBI group to multimodal TBI. Mice in the sham injury group were anesthetized and placed inside the multimodal TBI device without activating the overpressure chamber. We continued recording axonal activity for seven weeks after injury. **B.** Short-term increase in axonal tuning after multimodal TBI. The mean fraction of axonal segments that were significantly tuned ($P<0.01$, ANOVA test for tuning of segments, individual segment data not shown; see Methods for details) to the presented visual stimulus showed a significant group-by-time interaction between the TBI and sham control groups ($P=0.0017$, F-test). For the TBI group, the fraction was significantly increased by 74% (blue; $P=0.002$, Holm-adjusted) in the days before and after TBI, but not for the sham control group (gray). &&, $p<0.01$ for group-by-time interaction; **, $p<0.01$ for within-group comparison; n.s., not significant). For each experimental group, different lines (solid, dotted, dash-dotted) show data from different mice, error bars show the 95% confidence interval for the linear mixed-effects model, and the model mean values are connected with lines. **C.** Repeated recordings from the same FOV. Example mean images of the same FOV (mouse 6, TBI group) recorded 1 day before TBI (left), 4 days after TBI (middle), and 6 weeks after TBI (right). Activity movies from these recordings are shown in Supplementary Video 1. **D.** Mean $\Delta F/F_0$ traces across all detected segments for each FOV shown in **C**. Single trials (gray) and averages of five trials (black) are overlaid. Eight grating motion directions are indicated by arrows as shown above the traces. **E**. Sum of the $\Delta F/F_0$ traces in **D** shows an increase in response amplitudes after TBI (mean±s.d. for the 5 trials). **F.** Increase in the fraction of tuned segments for the TBI group. The percentage of tuned segments ($P<0.01$, one-way ANOVA for testing the tuning of segments to the stimulus; data for individual segments not shown; see Methods for details) was non-significantly increased for the TBI group over the weeks after injury and no increase was identified for the sham control group (no significant group-by-time interaction was detected, $P=0.092$, F-test). **G.** Gradual decrease in the number of detected segments after TBI. The number of segments per FOV showed a decrease in the TBI group (blue), with a model-estimated decrease of 15.2% from Week 1 to Week 7. A small decrease was identified in the sham control group (gray). These changes are consistent with reported findings on axonal degeneration in this multimodal TBI model. We note that the changes in our study were not significant for group and time interaction ($P=0.108$, F-test), suggesting that either more mice per group and/or longer recording periods are required to identify significant differences. For each group, data from single mice are represented by different markers (square, triangle, circle), and the model means are connected with lines.

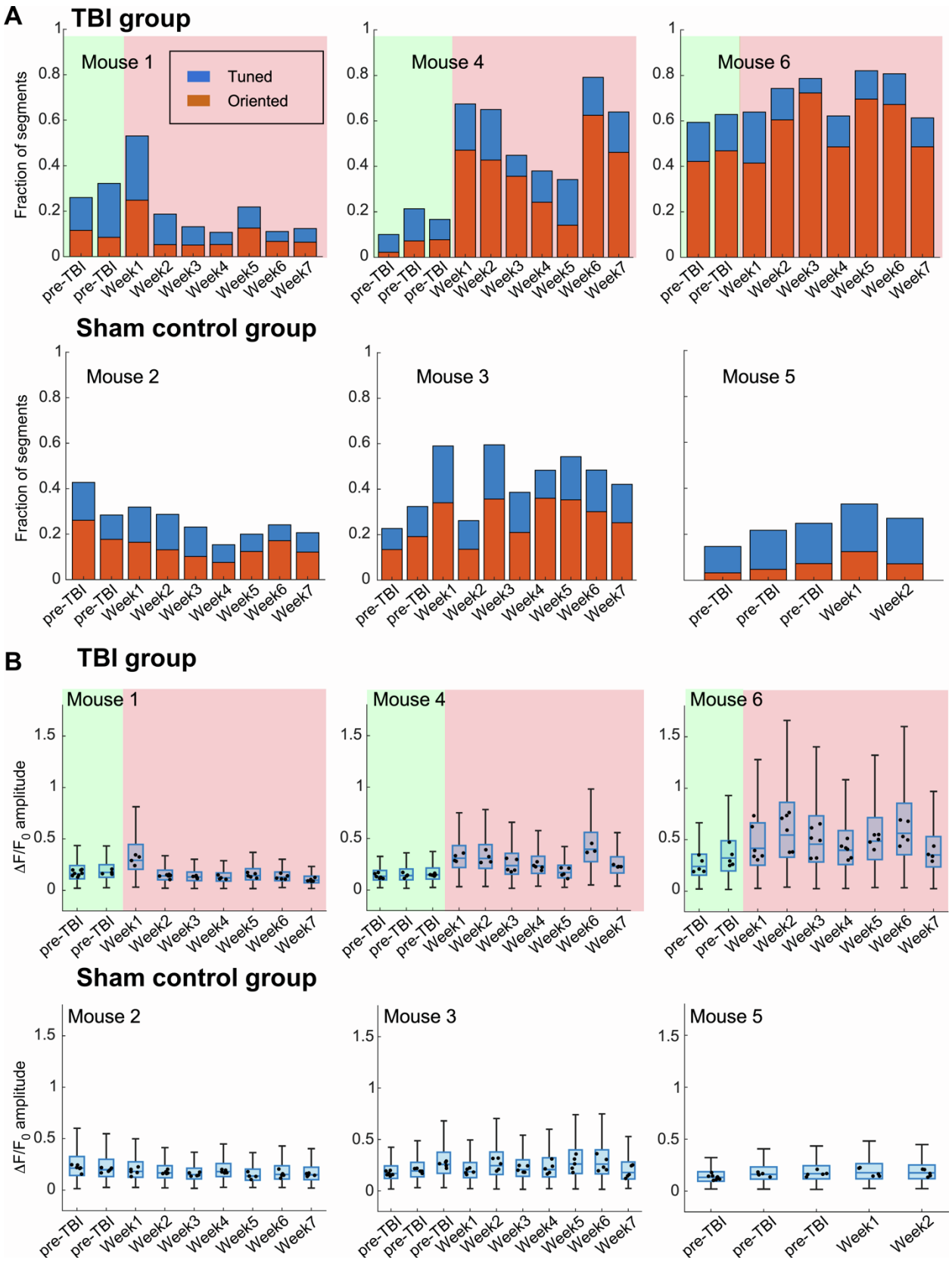
A
TBI group
Mouse 1
Tuned
Oriented
Mouse 4
Mouse 6
Fraction of segments
Sham control group
Mouse 2
Mouse 3
Mouse 5
pre-TBI
Week1
Week2
Week3
Week4
Week5
Week6
Week7
B
TBI group
Mouse 1
Mouse 4
Mouse 6
ΔF/F0 amplitude
Sham control group
Mouse 2
Mouse 3
Mouse 5

Supplementary Figure 2. Longitudinal monitoring of tuning, orientation, and response amplitudes for individual mice before and after multimodal TBI, related to Main Fig. 2. A. The fractions of tuned and oriented segments (blue and orange bars, respectively) from all recorded segments and all mice are shown for the multimodal TBI group (upper row), and sham injury group (bottom row). Green and red backgrounds indicate the pre- and post-TBI periods, respectively, for the TBI group. Data from all recorded FOVs on the same date were compiled to calculate the respective fractions. Note that data from mouse 5 were acquired for only 5 recording dates. **B.** Single-mouse $\Delta F/F_0$ response amplitudes are shown for the multimodal TBI (upper row), and sham control (bottom row) groups. Each box represents the 25-75 percentile range of the measured $\Delta F/F_0$ response amplitude from all recorded segments in a specific recording session. The whisker spans the smallest among the range of the entire data set, or 1.5 times the interquartile range. For each recording date, the median values from all recorded FOVs are overlaid on the boxplot data (black dots).

Methods S1. Matlab scripts and functions, which were used for the data analysis. Related to STAR Methods 1.

```
%this script receives a Matlab file of raw fluorescence recording,
%optionally after registration to fix small movements during recording.
%This file is called "reg"
% The recording was done at 30fps, where first a grey display is shown for
% 120 frames, and then the stimulus (1 of 8 directions) appears for 121
% frames.
%The code receives the pixels that identify the location of different
%axonal segments from the output of Suite2P, which is saved in the same
%folder as the recording data for each recorded FOV.

nCond=8;
nTrial=5;
nImPerBlock=241;
BasePeriod=(101:120);
StimPeriod=(121:241);
fs=30; %frames/sec
relevant_frames=1:nImPerBlock*nCond*nTrial; %these are the frames when the drifting grating stim was presented
neuropil_corr=0.7;

%% multiple FOVs
subdirs = uipickfiles('Output','Struct');
len=length(subdirs);
ROI_pile=[];
for m=1:len
   if subdirs(m).isdir
      files1=dir([subdirs(m).name,'/reg_movie_30Hz*']);
      files2=dir([subdirs(m).name,'/Fall.mat']);

      load([subdirs(m).name,filesep,files1(1,1).name]); %reg file
      load([subdirs(m).name,filesep,files2(1,1).name]); %Fall file

      num_seg_in_FOV(m)=size(F,1);
      %% load segmentation from Suite2P file, and apply it to the reg file
      if size(reg,3)~=10000
         beep
         error('wrong number of frames in reg file, check data')
      end
      ROI_list=struct('pixels',[],'fmean',[]);
      reg_mod=reshape(reg,[],size(reg,3));
      Fmean=zeros(size(F,1),size(reg,3));
```

```
        for i=1:size(Fmean,1)
            xpix=[];
            ypix=[];
            xpix=[xpix stat{i}.xpix];
            ypix=[ypix stat{i}.ypix];
            if sum(xpix==0)|sum(ypix==0) %if a pixels is at the edge
                ROI_list(i).pixels=sub2ind([size(reg,1) size(reg,2)],ypix+1, xpix+1);
            else
                ROI_list(i).pixels=sub2ind([size(reg,1) size(reg,2)],ypix, xpix);
            end
        end
        ROI_list=measure_neuropile_axon_suite2p(ROI_list,mean(reg,3));
        for i=1:size(F,1)
            ROI_list(i).fmean=mean(reg_mod(ROI_list(i).pixels,:),1);
            ROI_list(i).fmean_neuropile=mean(reg_mod(ROI_list(i).pixels_neuropile,:),1);
        end
    end
    ROI_pile=[ROI_pile ROI_list];
end

for i=1:length(ROI_pile)
    Fmean(i,:)=ROI_pile(i).fmean-neuropil_corr*ROI_pile(i).fmean_neuropile;
end
Fmean=Fmean(:,relevant_frames);

Fmean_org=Fmean;

nROI=size(Fmean,1);
Fmean=reshape(Fmean',[nImPerBlock,nCond,nTrial,nROI]); %transpose Fmean to fit the reshape format
df_f=rawf2df_f_init_f0(Fmean,BasePeriod);
df_f=reshape(df_f,[nImPerBlock,nCond,nTrial,nROI]);%transpose df/f to fit the reshape format

resp_avg=squeeze(mean(mean(df_f(StimPeriod,:,:,:),1),3));   % nstim x nROI
bestresp=max(resp_avg);
minresp=min(resp_avg);
resp_amplitude=bestresp-minresp;
for i=1:length(bestresp)
    ind=find(bestresp(i)==resp_avg(:,i));
    trace_mean=mean(squeeze(df_f(StimPeriod,ind,:,i)),2);
    trace_mean_sorted=sort(trace_mean,'descend');
    resp_peak(i)=mean(trace_mean_sorted(1:round(0.25*length(trace_mean_sorted))));
end
[IsRespond,IsOrient,p_resp,p_orient]=testResp(Fmean,BasePeriod,StimPeriod,0.05);
IsRespond=IsRespond&(bestresp>0.05);
IsOrient=IsOrient&(bestresp>0.05);
responsive_seg_num=sum(IsRespond)
oriented_seg_num=sum(IsOrient)
total_num_segments=length(IsRespond)

resp_amp_percentile=[myprctile(resp_amplitude,25) myprctile(resp_amplitude,50) myprctile(resp_amplitude,75)]
%correction for drifting of baseline which makes negative df/f

%%  fit tuning
ind=find(IsRespond);
angle=[45,90,135,180,225,270,315,360];
```

```
para_list=[];
for i=1:length(ind)
   para=fit_tuning(resp_avg(1:8,ind(i)),angle);
   para_list=[para_list,para];
end

save Combined_analysis_20201124
```

2.

```
%this script piles the data from individual FOVs to get piled data for a
%specific recording date.

close all;clear;clc
%%piled data
load('Combined_analysis_20211105.mat', 'num_seg_in_FOV', 'IsRespond', 'IsOrient','resp_amplitude','para_list')
total_num_segments=length(IsRespond)
resp_amp_median=median(resp_amplitude)
responsive_seg_num=sum(IsRespond)
oriented_seg_num=sum(IsOrient)
fraction_responsive=responsive_seg_num/total_num_segments
fraction_oriented=oriented_seg_num/total_num_segments
OSI_median=median([para_list.OSI])
DSI_median=median([para_list.DSI])

%% individual FOV data

switch length(num_seg_in_FOV)
    case 3
          median_resp_amp_per_FOV=[median(resp_amplitude(1:num_seg_in_FOV(1)))
median(resp_amplitude(1+num_seg_in_FOV(1):sum(num_seg_in_FOV(1:2))))...
          median(resp_amplitude(1+sum(num_seg_in_FOV(1:2)):sum(num_seg_in_FOV(1:3))))]

       IsResp_per_FOV=[sum(IsRespond(1:num_seg_in_FOV(1)))
sum(IsRespond(1+num_seg_in_FOV(1):sum(num_seg_in_FOV(1:2))))...
          sum(IsRespond(1+sum(num_seg_in_FOV(1:2)):sum(num_seg_in_FOV(1:3))))]

       IsOrient_per_FOV=[sum(IsOrient(1:num_seg_in_FOV(1)))
sum(IsOrient(1+num_seg_in_FOV(1):sum(num_seg_in_FOV(1:2))))...
          sum(IsOrient(1+sum(num_seg_in_FOV(1:2)):sum(num_seg_in_FOV(1:3))))]

        case 4
       median_resp_amp_per_FOV=[median(resp_amplitude(1:num_seg_in_FOV(1)))
median(resp_amplitude(1+num_seg_in_FOV(1):sum(num_seg_in_FOV(1:2))))...
          median(resp_amplitude(1+sum(num_seg_in_FOV(1:2)):sum(num_seg_in_FOV(1:3))))...
          median(resp_amplitude(1+sum(num_seg_in_FOV(1:3)):sum(num_seg_in_FOV(1:4))))]

       IsResp_per_FOV=[sum(IsRespond(1:num_seg_in_FOV(1)))
sum(IsRespond(1+num_seg_in_FOV(1):sum(num_seg_in_FOV(1:2))))...
          sum(IsRespond(1+sum(num_seg_in_FOV(1:2)):sum(num_seg_in_FOV(1:3))))...
          sum(IsRespond(1+sum(num_seg_in_FOV(1:3)):sum(num_seg_in_FOV(1:4))))]

       IsOrient_per_FOV=[sum(IsOrient(1:num_seg_in_FOV(1)))
sum(IsOrient(1+num_seg_in_FOV(1):sum(num_seg_in_FOV(1:2))))...
          sum(IsOrient(1+sum(num_seg_in_FOV(1:2)):sum(num_seg_in_FOV(1:3))))...
```

```
        sum(IsOrient(1+sum(num_seg_in_FOV(1:3)):sum(num_seg_in_FOV(1:4))))]

    case 5
        median_resp_amp_per_FOV=[median(resp_amplitude(1:num_seg_in_FOV(1)))
median(resp_amplitude(1+num_seg_in_FOV(1):sum(num_seg_in_FOV(1:2))))...
        median(resp_amplitude(1+sum(num_seg_in_FOV(1:2)):sum(num_seg_in_FOV(1:3))))...
        median(resp_amplitude(1+sum(num_seg_in_FOV(1:3)):sum(num_seg_in_FOV(1:4))))...
        median(resp_amplitude(1+sum(num_seg_in_FOV(1:4)):end))]

        IsResp_per_FOV=[sum(IsRespond(1:num_seg_in_FOV(1)))
sum(IsRespond(1+num_seg_in_FOV(1):sum(num_seg_in_FOV(1:2))))...
        sum(IsRespond(1+sum(num_seg_in_FOV(1:2)):sum(num_seg_in_FOV(1:3))))...
        sum(IsRespond(1+sum(num_seg_in_FOV(1:3)):sum(num_seg_in_FOV(1:4))))...
        sum(IsRespond(1+sum(num_seg_in_FOV(1:4)):end))]

        IsOrient_per_FOV=[sum(IsOrient(1:num_seg_in_FOV(1)))
sum(IsOrient(1+num_seg_in_FOV(1):sum(num_seg_in_FOV(1:2))))...
        sum(IsOrient(1+sum(num_seg_in_FOV(1:2)):sum(num_seg_in_FOV(1:3))))...
        sum(IsOrient(1+sum(num_seg_in_FOV(1:3)):sum(num_seg_in_FOV(1:4))))...
        sum(IsOrient(1+sum(num_seg_in_FOV(1:4)):end))]

    case 6
        median_resp_amp_per_FOV=[median(resp_amplitude(1:num_seg_in_FOV(1)))
median(resp_amplitude(1+num_seg_in_FOV(1):sum(num_seg_in_FOV(1:2))))...
        median(resp_amplitude(1+sum(num_seg_in_FOV(1:2)):sum(num_seg_in_FOV(1:3))))...
        median(resp_amplitude(1+sum(num_seg_in_FOV(1:3)):sum(num_seg_in_FOV(1:4))))...
        median(resp_amplitude(1+sum(num_seg_in_FOV(1:4)):sum(num_seg_in_FOV(1:5))))...
        median(resp_amplitude(1+sum(num_seg_in_FOV(1:5)):end))]

        IsResp_per_FOV=[sum(IsRespond(1:num_seg_in_FOV(1)))
sum(IsRespond(1+num_seg_in_FOV(1):sum(num_seg_in_FOV(1:2))))...
        sum(IsRespond(1+sum(num_seg_in_FOV(1:2)):sum(num_seg_in_FOV(1:3))))...
        sum(IsRespond(1+sum(num_seg_in_FOV(1:3)):sum(num_seg_in_FOV(1:4))))...
        sum(IsRespond(1+sum(num_seg_in_FOV(1:4)):sum(num_seg_in_FOV(1:5))))...
        sum(IsRespond(1+sum(num_seg_in_FOV(1:5)):end))]

        IsOrient_per_FOV=[sum(IsOrient(1:num_seg_in_FOV(1)))
sum(IsOrient(1+num_seg_in_FOV(1):sum(num_seg_in_FOV(1:2))))...
        sum(IsOrient(1+sum(num_seg_in_FOV(1:2)):sum(num_seg_in_FOV(1:3))))...
        sum(IsOrient(1+sum(num_seg_in_FOV(1:3)):sum(num_seg_in_FOV(1:4))))...
        sum(IsOrient(1+sum(num_seg_in_FOV(1:4)):sum(num_seg_in_FOV(1:5))))...
        sum(IsOrient(1+sum(num_seg_in_FOV(1:5)):end))]

    case 7
        median_resp_amp_per_FOV=[median(resp_amplitude(1:num_seg_in_FOV(1)))
median(resp_amplitude(1+num_seg_in_FOV(1):sum(num_seg_in_FOV(1:2))))...
        median(resp_amplitude(1+sum(num_seg_in_FOV(1:2)):sum(num_seg_in_FOV(1:3))))...
        median(resp_amplitude(1+sum(num_seg_in_FOV(1:3)):sum(num_seg_in_FOV(1:4))))...
        median(resp_amplitude(1+sum(num_seg_in_FOV(1:4)):sum(num_seg_in_FOV(1:5))))...
        median(resp_amplitude(1+sum(num_seg_in_FOV(1:5)):sum(num_seg_in_FOV(1:6))))...
        median(resp_amplitude(1+sum(num_seg_in_FOV(1:6)):end))]

        IsResp_per_FOV=[sum(IsRespond(1:num_seg_in_FOV(1)))
sum(IsRespond(1+num_seg_in_FOV(1):sum(num_seg_in_FOV(1:2))))...
        sum(IsRespond(1+sum(num_seg_in_FOV(1:2)):sum(num_seg_in_FOV(1:3))))...
        sum(IsRespond(1+sum(num_seg_in_FOV(1:3)):sum(num_seg_in_FOV(1:4))))...
```

```
        sum(IsRespond(1+sum(num_seg_in_FOV(1:4)):sum(num_seg_in_FOV(1:5))))...
        sum(IsRespond(1+sum(num_seg_in_FOV(1:5)):sum(num_seg_in_FOV(1:6))))...
        sum(IsRespond(1+sum(num_seg_in_FOV(1:6)):end))]

    IsOrient_per_FOV=[sum(IsOrient(1:num_seg_in_FOV(1)))
sum(IsOrient(1+num_seg_in_FOV(1):sum(num_seg_in_FOV(1:2))))...
        sum(IsOrient(1+sum(num_seg_in_FOV(1:2)):sum(num_seg_in_FOV(1:3))))...
        sum(IsOrient(1+sum(num_seg_in_FOV(1:3)):sum(num_seg_in_FOV(1:4))))...
        sum(IsOrient(1+sum(num_seg_in_FOV(1:4)):sum(num_seg_in_FOV(1:5))))...
        sum(IsOrient(1+sum(num_seg_in_FOV(1:5)):sum(num_seg_in_FOV(1:6))))...
        sum(IsOrient(1+sum(num_seg_in_FOV(1:6)):end))]

    case 8
    median_resp_amp_per_FOV=[median(resp_amplitude(1:num_seg_in_FOV(1)))
median(resp_amplitude(1+num_seg_in_FOV(1):sum(num_seg_in_FOV(1:2))))...
        median(resp_amplitude(1+sum(num_seg_in_FOV(1:2)):sum(num_seg_in_FOV(1:3))))...
        median(resp_amplitude(1+sum(num_seg_in_FOV(1:3)):sum(num_seg_in_FOV(1:4))))...
        median(resp_amplitude(1+sum(num_seg_in_FOV(1:4)):sum(num_seg_in_FOV(1:5))))...
        median(resp_amplitude(1+sum(num_seg_in_FOV(1:5)):sum(num_seg_in_FOV(1:6))))...
        median(resp_amplitude(1+sum(num_seg_in_FOV(1:6)):sum(num_seg_in_FOV(1:7))))...
        median(resp_amplitude(1+sum(num_seg_in_FOV(1:7)):end))]

    IsResp_per_FOV=[sum(IsRespond(1:num_seg_in_FOV(1)))
sum(IsRespond(1+num_seg_in_FOV(1):sum(num_seg_in_FOV(1:2))))...
        sum(IsRespond(1+sum(num_seg_in_FOV(1:2)):sum(num_seg_in_FOV(1:3))))...
        sum(IsRespond(1+sum(num_seg_in_FOV(1:3)):sum(num_seg_in_FOV(1:4))))...
        sum(IsRespond(1+sum(num_seg_in_FOV(1:4)):sum(num_seg_in_FOV(1:5))))...
        sum(IsRespond(1+sum(num_seg_in_FOV(1:5)):sum(num_seg_in_FOV(1:6))))...
        sum(IsRespond(1+sum(num_seg_in_FOV(1:6)):sum(num_seg_in_FOV(1:7))))...
        sum(IsRespond(1+sum(num_seg_in_FOV(1:7)):end))]

    IsOrient_per_FOV=[sum(IsOrient(1:num_seg_in_FOV(1)))
sum(IsOrient(1+num_seg_in_FOV(1):sum(num_seg_in_FOV(1:2))))...
        sum(IsOrient(1+sum(num_seg_in_FOV(1:2)):sum(num_seg_in_FOV(1:3))))...
        sum(IsOrient(1+sum(num_seg_in_FOV(1:3)):sum(num_seg_in_FOV(1:4))))...
        sum(IsOrient(1+sum(num_seg_in_FOV(1:4)):sum(num_seg_in_FOV(1:5))))...
        sum(IsOrient(1+sum(num_seg_in_FOV(1:5)):sum(num_seg_in_FOV(1:6))))...
        sum(IsOrient(1+sum(num_seg_in_FOV(1:6)):sum(num_seg_in_FOV(1:7))))...
        sum(IsOrient(1+sum(num_seg_in_FOV(1:7)):end))]
end
```

3.

```
function df_f=rawf2df_f_init_f0(f,f0_range)
% f2=reshape(f,121,[]);
ss=size(f);
if (length(ss)==2)
   ss(3)=1;
   ss(4)=1;
end
f0=zeros(ss);

for  i=1:ss(3)
   for j=1:ss(4)
      f0(:,1,i,j)=mean(f(f0_range,1,i,j));
      for k=2:ss(2)
         f0(:,k,i,j)=f0(:,1,i,j);
```

```
        end
    end
end

f0=reshape(f0,ss(1),[]);
f=reshape(f,ss(1),[]);

% f0=mean(f(f0_range,:));

% f0=repmat(f0,[ss(1),1]);
df_f=(f-f0)./f0;
df_f=reshape(df_f,ss);
```

4.

```
function [IsRespond,IsOrient,p_resp,p_orient]=testResp(fmean,BasePeriod,StimPeriod,threshold)
%this script runs an ANOVA test to find tuned and oriented segments
%fmean: 4D array nImPerBlock x nCond x nTrial x nROI

nImPerBlock=size(fmean,1);
nCond=size(fmean,2);
nTrial=size(fmean,3);
nROI=size(fmean,4);

IsRespond=false(1,nROI);
IsOrient=false(1,nROI);

%%  test for response,  ANOVA P<0.01

fbase=mean(fmean(BasePeriod,:,:,:));
fbase=reshape(fbase,[],nROI);åå
fresp=mean(fmean(StimPeriod,:,:,:));
fresp=reshape(fresp,[],nROI);
group=[zeros(nTrial*nCond,1);repmat((1:nCond)',[nTrial,1])];
ftestmatrix=[fbase;fresp];

for i=1:nROI
    p_resp(i)=anova1(ftestmatrix(:,i),group,'off');
    if p_resp(i)<threshold
        IsRespond(i)=true;
    else
        IsRespond(i)=false;
    end
end

%%  test for Orientation, ANOVA P<0.01
fresp=mean(fmean(StimPeriod,:,:,:));
fresp=reshape(fresp,[],nROI);
group=repmat((1:nCond)',[nTrial,1]);
for i=1:nROI
    p_orient(i)=anova1(fresp(:,i),group,'off');
    if (p_orient(i)<threshold) && (IsRespond(i)==1)
        IsOrient(i)=true;
    else
        IsOrient(i)=false;
    end
end
```